ILASS Americas 22nd Annual Conference on Liquid Atomization and Spray Systems, Cincinnati, OH, May 2010

Large Eddy Simulations of Temporal Mixing Layers under Supercritical Thermodynamic Conditions: O_2/H_2

Ezgi S. Taşkinoğlu[1] and Josette Bellan[1,2]
California Institute of Technology[1], Pasadena CA 91125
Jet Propulsion Laboratory[2], California Institute of Technology, Pasadena CA 91109-8099

Abstract

A Direct Numerical Simulation (DNS) database of supercritical temporal mixing layer simulations of binary mixtures is studied to identify the Large Eddy Simulation (LES) subgrid scale model needs for high pressure flows. For the oxygen/hydrogen (OH) mixture studied here, an earlier *a priori* study showed that in addition to the usual subgrid scale flux terms, a new term in the filtered energy equation must be modeled. A model formulation was proposed for this term called heat flux correction (q-correction), but the model was only partially successful in the *a priori* tests. In this study, the earlier *a priori* analysis is revisited to investigate the reasons for the limited success of the previously proposed model for the q-correction. In addition, a new modeling strategy is proposed and examined *a priori*. Finally, an *a posteriori* study is conducted to test the viability of the newly proposed model.

1 Introduction

The operating pressures of advanced propulsion devices, such as advanced gas turbine, diesel engines and liquid rockets, exceed the thermodynamic critical pressure of the fuel or oxidizer during many instances of most of their operating conditions. When the critical pressure of the fluid is exceeded, the fluid disintegration and mixing processes exhibit distinctive features not present under atmospheric conditions. One of these features is the appearance of regions of sharp density gradients observed both experimentally and numerically [15, 11]. The high density-gradient magnitude regions play a crucial role in determining turbulence characteristics of the fluid by delaying the transition and redistributing turbulence[4, 11].

Direct numerical simulation (DNS) studies, where all scales of the flow motion are resolved, were conducted both for pre-transitional [11], and transitional temporal mixing layers under supercritical conditions [14]. However, for fully turbulent supercritical flows at high pressures, large eddy simulation (LES), where only the large scales are resolved while small scales are modeled, is less computationally intensive and thus has a better chance of being adopted for engineering purposes. The LES equations are obtained by filtering of the DNS equations, an operation which yields unclosed terms that can not be computed from the filtered flow field, so that explicit modeling must be utilized to reinsert the missing small-scale effects in the equations, unless these terms are shown negligible, in which case simplifying assumptions can be used. An earlier *a priori* study of a DNS database has shown that some of the unclosed terms assumed to be negligible for atmospheric pressure flows can not be neglected for high pressure flows [18]. These terms, one in momentum equation, $\nabla[\bar{p}-p(\bar{\phi})]$ (pressure correction), and one in the energy equation, $\nabla\cdot\left[\overline{q_{IK}(\phi)}-q_{IK}(\bar{\phi})\right]$(heat flux ($q$) correction), has been found to have significant contributions to the corresponding LES equation [18].

The focus of the current study is the *a priori* and *a posteriori* analyses for the q-correction models required for the oxygen/hydrogen (OH) O_2/H_2 system.

2 Governing Equations

The LES equations were derived by Selle *et. al.*[18] from the conservation equations by spatial filtering. The filtering operation is defined as

$$\overline{\psi}(\vec{x})=\int_V \psi(\vec{y})G(\vec{x}-\vec{y})d\vec{y}, \tag{1}$$

where G is the filter function and V is the filtering volume; G has the property that for a spatially invariant function, the filtered function is identical to the unfiltered one. For compressible flows, Favre filtering is used, defined as $\tilde{\psi}=\overline{\rho\psi}/\bar{\rho}$ where ρ is the density. The variance of two quantities φ and θ is defined as $\vartheta(\overline{\varphi},\overline{\theta})=\overline{\varphi\theta}-\overline{\varphi}\ \overline{\theta}$ or $\vartheta(\widetilde{\varphi},\widetilde{\theta})=\widetilde{\varphi\theta}-\widetilde{\varphi}\widetilde{\theta}$, depending on the filtering. The governing equations are written for the conservative variables $\phi=\{\rho,\rho u_i,\rho e_t,\rho Y_\alpha\}$, where u_i is the velocity component in the x_i-direction spatial coordinate, e_t is the total energy, Y_α and X_α are the mass fraction and mole fraction of species α, and T is the temperature.

The filtered governing equations are obtained under the assumption that filtering and differentiation commute (the top-hat filter is used here for which the operations commute except near boundaries). These equations contain several unclosed terms that cannot be directly computed from the filtered flow field. To compute these terms, two closure approaches are pursued: explicit models for the subgrid scale (SGS) fluxes, and simplifying assumptions for the remaining terms. The assumptions and models are assessed in Selle *et. al.*[18] on a DNS database of a binary non-reacting temporal mixing layer. After omitting the negligible terms, the filtered equations become:

$$\frac{\partial\bar{\rho}}{\partial t}+\frac{\partial(\bar{\rho}\tilde{u}_j)}{\partial x_j}=0, \tag{2}$$

$$\begin{aligned}\frac{\partial(\bar{\rho}\tilde{u}_i)}{\partial t}+\frac{\partial(\bar{\rho}\tilde{u}_i\tilde{u}_j)}{\partial x_j} &= -\frac{\partial p\left(\overline{\phi}\right)}{\partial x_i}+\frac{\partial\sigma_{ij}\left(\overline{\phi}\right)}{\partial x_j}\\ &\quad -\frac{\partial}{\partial x_j}\left(\bar{\rho}\tau_{ij}\right)\\ &\quad -\frac{\partial}{\partial x_i}\left[\bar{p}-p\left(\overline{\phi}\right)\right],\end{aligned} \tag{3}$$

$$\begin{aligned}\frac{\partial(\bar{\rho}\tilde{e}_t)}{\partial t}+\frac{\partial(\bar{\rho}\tilde{e}_t\tilde{u}_j)}{\partial x_j} &= -\frac{\partial p\left(\overline{\phi}\right)\tilde{u}_j}{\partial x_j}-\frac{\partial q_{IKj}\left(\overline{\phi}\right)}{\partial x_j}\\ &\quad +\frac{\partial(\sigma_{ij}\left(\overline{\phi}\right)\tilde{u}_i)}{\partial x_j}-\frac{\partial}{\partial x_j}\left(\bar{\rho}\zeta_j\right)-\frac{\partial\left(\bar{\rho}\tau_{ij}\widetilde{u}_i\right)}{\partial x_j}\\ &\quad -\frac{\partial}{\partial x_j}\left[\bar{q}_{IKj}-q_{IKj}\left(\overline{\phi}\right)\right],\end{aligned} \tag{4}$$

$$\frac{\partial(\bar{\rho}\tilde{Y}_\alpha)}{\partial t}+\frac{\partial(\bar{\rho}\tilde{Y}_\alpha\tilde{u}_j)}{\partial x_j}=-\frac{\partial j_{\alpha j}\left(\overline{\phi}\right)}{\partial x_j}-\frac{\partial}{\partial x_j}\left(\bar{\rho}\eta_{\alpha j}\right), \tag{5}$$

where the SGS fluxes are

$$\begin{aligned}\tau_{ij} &= \vartheta(\widetilde{u}_i,\widetilde{u}_j), \quad \zeta_j = \vartheta(\tilde{h},\tilde{u}_j),\\ \eta_{\alpha j} &= \vartheta(\widetilde{Y}_\alpha,\widetilde{u}_j) \text{ with } \sum_{\alpha=1}^{N}\eta_{\alpha j}=0, \end{aligned} \quad (6)$$

and the additional SGS terms modeled *a priori* by Selle *et. al.*[18] are $\nabla\left[\bar{p}-p\left(\overline{\phi}\right)\right]$ (pressure correction), and $\nabla\cdot\left[\bar{q}_{IK}-q_{IK}\left(\overline{\phi}\right)\right]$ (q-correction). Selle *et al.*. [18] showed that for O_2/H_2 (OH) system, pressure correction is negligible, whereas the q-correction must be modeled.

In equations (2) - (5), t is the time, $\boldsymbol{\sigma}$ is the viscous stress tensor, $\mathbf{q}_{IK}$ is the Irwing-Kirkwood (subscript IK) heat flux, $e=e_t-e_K$ is the internal energy, $e_K=u_iu_i/2$ is the kinetic energy, N is the number of species and $\mathbf{j}_\alpha$ is the species-mass flux of species α. Also,

$$\sum_{\alpha=1}^{N} Y_\alpha = 1, \quad \sum_{\alpha=1}^{N} j_{\alpha j} = 0. \quad (7)$$

Here, the Einstein summation is used for roman indices (i,j,k), but not for Greek indices (α,β). The thermodynamic variables are functions of the LES flow field $\overline{\phi}$:

$$\begin{aligned} e &= e\left(\overline{\phi}\right), \quad p=p\left(\overline{\phi}\right), \quad Y=Y\left(\overline{\phi}\right), \quad (8)\\ T &= T\left(\overline{\phi}\right), \quad h=h\left(\overline{\phi}\right) \quad (9)\end{aligned}$$

where p, T and the enthalpy $h=e+p/\rho$ are computed from the EOS; likewise, the fluxes are functions of $\overline{\phi}$:

$$\sigma_{ij}=\sigma_{ij}\left(\overline{\phi}\right), \quad j_{\alpha j}=j_{\alpha j}\left(\overline{\phi}\right), \quad q_{IKj}=q_{IKj}\left(\overline{\phi}\right). \quad (10)$$

For a Newtonian fluid,

$$\begin{aligned}\sigma_{ij} &= \mu\left(\frac{\partial u_i}{\partial x_j}+\frac{\partial u_j}{\partial x_i}-\frac{2}{3}\frac{\partial u_k}{\partial x_k}\delta_{ij}\right), \quad (11)\\ S_{ij} &= \frac{1}{2}\left(\frac{\partial u_i}{\partial x_j}+\frac{\partial u_j}{\partial x_i}\right), \quad (12)\end{aligned}$$

where μ is the viscosity and S_{ij} is the rate-of-strain tensor.

The species-mass and heat fluxes originate in the fluctuation-dissipation theory [8] which is consistent with non-equilibrium thermodynamics, converges to kinetic theory in the low-pressure limit, and relates fluxes and forces from first principles. For a binary-species system (light species 1, heavy species 2), the species-mass and heat fluxes, including Soret and Dufour effects [7], are:

$$\begin{aligned}\mathbf{j}_2(\overline{\psi}) &= B_Y(\overline{\psi})\nabla Y_2\left(\overline{\phi}\right)+B_T(\overline{\psi})\nabla T\left(\overline{\phi}\right)\\ &\quad + B_P(\overline{\psi})\nabla p\left(\overline{\phi}\right), \quad (13)\\ \mathbf{q}_{IK}(\overline{\psi}) &= C_Y(\overline{\psi})\nabla Y_2\left(\overline{\phi}\right)+C_T(\overline{\psi})\nabla T\left(\overline{\phi}\right)\\ &\quad + C_P(\overline{\psi})\nabla p\left(\overline{\phi}\right), \quad (14)\end{aligned}$$

where $\overline{\psi}\equiv\psi(\overline{\phi})$ and functionally

$$\begin{aligned} B_Y &\equiv -\rho D\alpha_D, \quad (15)\\ C_Y &\equiv -\rho D\alpha_D\alpha_{IK}R_uT\frac{m}{m_1m_2}, \quad (16)\\ B_T &\equiv -\alpha_{BK}Y_1Y_2\frac{\rho D}{T}, \quad (17)\\ C_T &\equiv -\lambda-\rho D\alpha_{IK}\alpha_{BK}R_u\frac{m}{m_1m_2}Y_1Y_2, \quad (18)\\ B_P &\equiv -\rho D\frac{Y_1Y_2}{R_uT}\frac{m_2m_1}{m}\Lambda, \quad (19)\\ C_P &\equiv -\rho D\alpha_{IK}\Lambda Y_1Y_2. \quad (20)\end{aligned}$$

In equations (16)-(20)

$$\alpha_{BK}=\alpha_{IK}-\alpha_h, \quad \alpha_h=\frac{1}{R_uT}\frac{m_2m_1}{m}\Theta, \quad (21)$$

$$\begin{aligned}\Lambda &\equiv \left(\frac{1}{m_2}\frac{\partial v}{\partial X_2}-\frac{1}{m_1}\frac{\partial v}{\partial X_1}\right), \quad (22)\\ \Theta &\equiv \left(\frac{1}{m_2}\frac{\partial (mh)}{\partial X_2}-\frac{1}{m_1}\frac{\partial (mh)}{\partial X_1}\right), \quad (23)\end{aligned}$$

$$\alpha_D \equiv 1+X_\alpha\frac{\partial \ln\gamma_\alpha}{\partial X_\beta}, \quad (24)$$

where λ is the thermal conductivity with $\lim_{p\to 0}\lambda=\lambda_{KT}$ as discussed in Harstad *et. al.* [7] and the subscript KT denotes the kinetic theory, R_u is the universal gas constant, m is the mixture molar mass, and v is the molar volume with $v=m/\rho$. For species α, m_α is the species-α molar mass, $X_\alpha=mY_\alpha/m_\alpha$, and γ_α is the fugacity. Furthermore, α_{IK} is the IK form of the thermal diffusion factor, α_{BK} is the Bearman-Kirkwood (BK) form of the thermal diffusion factor, D is the binary diffusion coefficient and α_D is the mass diffusion factor.

2.1 Equation of state

The pressure is calculated from the well-known Peng-Robinson (PR) EOS, given T and the PR molar volume (v_{PR}), as

$$p=\frac{R_uT}{(v_{PR}-b_m)}-\frac{a_m}{(v_{PR}^2+2b_mv_{PR}-b_m^2)}, \quad (25)$$

where a_m and b_m are functions of T and X_α whose mathematical form is given in detail in Miller *et.*

al. [11] and Okong'o *et. al.* [14]. At high pressures, v_{PR} may differ significantly from the actual molar volume v [16]. Both v_{PR} and the volume shift ($v_S = v - v_{PR}$) can be calculated from the PR EOS given p, T and X_α [5]. All thermodynamic quantities, including α_D, h, $C_p = (\partial h/\partial T)_{p,X}$ and the speed of sound (a_s), are calculated from the EOS using standard thermodynamic relations [11, 12, 14]. The implementation of the EOS to calculate p and T from ρ, e and Y_α uses an iterative scheme [14] for OH system. The pure species properties are listed in table 1. For each layer, species 1 and 2 initially reside in the upper and lower stream, respectively.

2.2 Transport coefficients

The viscosity, the Schmidt number ($Sc = \mu/(\rho\alpha_D D)$) and the Prandtl number ($\Pr = \mu C_p/(m\lambda)$) were calculated from high-pressure single-species transport properties using mixing rules, as in Harstad and Bellan[6]. The calculated values were correlated, as summarized in table 2, and these correlations are then used to compute the transport properties μ, D and λ. The relationship between α_{BK} and α_{IK} stated in equation 21 means that either one can be specified, and the other then calculated.

2.3 SGS-flux models

To close the LES governing equations SGS fluxes must be modeled. The three basic constant-coefficient models for the SGS fluxes (τ_{ij}, $\eta_{\alpha j}$, ζ_j) are the SMC, GRC and SSC models[13]. The Smagorinsky (SMC) model is based on the gradient-diffusion (eddy-viscosity) concept[19]. The SGS fluxes in equation 6 are

$$\vartheta_{SM}(\widetilde{\psi}_m, \tilde{u}_j) = -C_{SM}\bar{\Delta}^2 S\left(\bar{\phi}\right)\frac{1}{2}\frac{\partial\widetilde{\psi}_m}{\partial x_j}, \qquad \psi_m \neq u_j \tag{26}$$

with τ_{ij} modeled in trace-free form as

$$\tau_{ij} - \frac{1}{3}\tau_{kk}\delta_{ij} = -C_{SM}\bar{\Delta}^2 S\left(\bar{\phi}\right)\left[S_{ij}\left(\bar{\phi}\right) - \frac{1}{3}S_{kk}\left(\bar{\phi}\right)\delta_{ij}\right] \tag{27}$$

where $S^2(\phi) = S_{ij}(\phi)\,S_{ij}(\phi)$. The Yoshizawa (YO)[23] model for τ_{kk} is

$$\tau_{kk} = C_{YO}\bar{\Delta}^2 S^2\left(\bar{\phi}\right). \tag{28}$$

The Gradient (GRC) model, derived from a Taylor series expansion[13, 2], is

$$\vartheta_{GR}(\widetilde{\psi}_m, \widetilde{\psi}_n) = C_{GR}\bar{\Delta}^2\frac{\partial\widetilde{\psi}_m}{\partial x_k}\frac{\partial\widetilde{\psi}_n}{\partial x_k}. \tag{29}$$

(Note: $\vartheta(\tilde{u}_1, \tilde{u}_1) = \tau_{11}$, $\vartheta(\tilde{u}_2, \tilde{u}_2) = \tau_{22}$, $\vartheta(\tilde{u}_3, \tilde{u}_3) = \tau_{33}$.) Theoretically, C_{GR} is proportional to the moments of inertia of the filtering volume; for a cubic top-hat filter $C_{GR} = 1/12$[13].

The Scale-Similarity (SSC) model, which postulates similarity between the SGS and the small resolved scale[1] is

$$\vartheta_{SS}(\widetilde{\psi}_m, \widetilde{\psi}_n) = C_{SS}\left(\widehat{\widetilde{\psi}_m\widetilde{\psi}_n} - \widehat{\widetilde{\psi}}_m\widehat{\widetilde{\psi}}_n\right), \tag{30}$$

where the overhat ($\widehat{\ }$) denotes (unweighted) filtering at the test-filter level $\hat{\Delta}$. The test filter width considered is $\hat{\Delta}/\bar{\Delta} = 2$, as it is generally recommended. While scale-similarity would imply that $C_{SS} = 1$, the actual value is filter-width dependent[10, 17, 13].

Because of the highly dissipative nature of the SMC model, we employed the Smagorinsky model with dynamic modeling. The premise of dynamic modeling is that a scale similarity exists, and thus the SGS behavior may be deduced from that of the small resolved scales. A test filter is introduced, $\hat{\Delta}$, such that $\hat{\Delta} > \bar{\Delta}$, and through the action of double filtering, $\widehat{\bar{\Delta}}$, a field with scales larger than the resolved field is generated. Here $\widehat{\bar{\Delta}}$ is the effective filter width, not actually used for filtering, that corresponds to filtering at $\bar{\Delta}$ followed by filtering at $\hat{\Delta}$, and the value of which depends on the filter type. For the top-hat filter used here both for the grid and test filter, $\widehat{\bar{\Delta}}$ is optimally approximated by $\widehat{\bar{\Delta}}^2 = \bar{\Delta}^2 + \hat{\Delta}^2$ ([22]). The essence of dynamic modeling is to relate the grid-level SGS flux and the test-level SGS flux to the test-level resolved flux using Germano's identity [3]. Following Lilly [9], a least-squares method is used to minimize the error in computing the coefficient from an overdetermined equation set.

In addition, a dynamic mixed model calculation, where the Smagorinsky model is used in combination with the gradient model (MGRD) is also used. The dynamic mixed model follows the approach of Vreman [22]: the coefficient of the SM model is dynamically calculated and that of the Gradient model is kept constant at its theoretical value.

3 Flow configuration and numerical method

The flow configuration is shown in fig. 1, and initial conditions are tabulated in table 3. In the table, subscript 0 labels the initial condition, 1 labels the upper stream and 2 labels the lower stream; T is temperature; p is pressure; L_i, $i = 1, 2, 3$ represents the dimension of the physical domain in the i^{th} direction; Δx is the DNS grid size; t^*_{tr} is the transitional time; and $Re_{m,tr}$ is the momentum-thickness based Reynolds number at transition.

The numerical methods have been described in

detail elsewhere[18].

4 *A priori* analysis

In the *a priori* study, the r.m.s. activity of terms in the conservation equations are examined, and the significant terms in the equations are identified, first, by comparing the domain r.m.s. values of each term, and then by examining their variation in the x_2 nonhomogeneous direction.

4.1 Domain r.m.s. activity

The domain r.m.s. of terms in the conservation equations are computed at various time steps and tabulated in table 4 through table 7. The tables list the terms ranked from that having the most significant contribution to that with the least contribution at $t^* = t^*_{tr} = 150$. Accordingly, in the x_1 momentum equation the most significant term is the advection term followed by the pressure and viscous work terms and the subgrid term. The pressure correction term is less than 3% of the advection term. This trend is the same at other time steps (table 4). The maximum pressure correction contribution is at $t^* = 50$, approximately 4%. In the x_2-momentum equation the contribution from pressure correction term becomes considerable: the maximum is at $t^* = 25$ with 34% and decreased towards transition time to 8%. In the x_2-momentum equation, although the terms rank similarly with these in the x_1-momentum equation at t^*_{tr}, differences appear at the earlier stages when the pressure correction term becomes more significant than both the viscous and the subgrid term (table 5). In the x_3-momentum equation, the pressure correction term is the third in order of importance even at the transition time (20%), and competes with the advection term at $t^* = 25$ (table 6). In the energy equation, the leading order terms are the heat flux and advection, the subgrid stresses and the pressure work at all listed times. The q-correction is comparable to the pressure work and 30% of the leading order term. The maximum contribution from the q-correction is observed at $t^* = 50$ as 49%. In the species equation, the maximum contribution of the mass-species flux correction is less than 4% (not shown).

Thus, for each conservation equation, the significant contribution of the correction term is required throughout the flow evolution. It is, therefore necessary to investigate the effect of q-correction not only at the transition time but also at the earlier stages of flow evolution.

4.2 x_2-r.m.s. activity

To complement the domain r.m.s. activity study, the x_2 r.m.s. of the leading order terms in the filtered energy equation are compared, and the results are plotted in fig. 2 at two time steps, $t^* = 50$, $t^* = 150$. The advection term has the largest contribution. It is followed by the pressure work and the subgrid term, which compete at the early times of the simulation with the pressure work becoming dominant at $t^* = 100$ (not shown) and $t^* = 150$. The contribution of the heat flux is approximately half of that of the subgrid term. And the divergence of the heat flux difference is half of that of the heat flux term. All other terms in the energy equation are small in comparison, and therefore not shown. Two main conclusions are: first, the q-correction is necessary particularly at the early stages of the layer development; second, its contribution is larger than the viscous term but smaller than subgrid term.

To gain a better understanding, the heat flux equation, eq. 14, is closely examined. Equation 14 has three contributions due to concentration, temperature and pressure gradients. And each contribution is composed of a gradient term ($\nabla A_j(\phi)$) and a coefficient term ($C_{A_j}(\phi)$) associated with the corresponding gradient. In compact form, it can be written as:

$$\mathbf{q}_{IK}(\phi) = \sum_{j=1}^{j=3} C_{A_j}(\phi) \nabla A_j(\phi) \qquad (31)$$

where, j refers to the each contribution. The x_2-r.m.s. difference between the filtered heat flux divergence and the heat flux divergence calculated from the filtered flow field for each heat-flux contribution is compared in fig. 3 at time steps $t^* = 50$ and 150. The maximum contribution is from the species mass term. The contribution from the temperature term is comparable with that of the pressure term and less than one fifth of that of the species mass term.

The coefficient and the gradients of each contribution are also separately examined. The gradient of species mass contribution is the smallest but its coefficient is the largest among all other coefficients (not shown). The largest difference between the filtered contribution and the contribution computed using the filtered flow field is obtained from the pressure gradient term, but since its coefficient is very small, the overall contribution to heat flux due to the pressure is small compared to that of the species mass term. Based on the high coefficient values of the species mass contribution, which is the main contributor of the heat flux (see fig. 3), it is natural to hypothesize that the modeling effort should focus on the coefficients. This strategy is the followed approach of Selle *et al.*.[18]. Although the coefficient representation of that model compares well

with that of DNS data, the heat flux representation was deemed unsatisfactory. To investigate this paradox, we examine both the mean and the r.m.s. of the difference between the filtered contribution and the contribution computed using the filtered flow field due to the species mass gradient from the standpoint of coefficients and total contribution to the q-correction. Figure 4(a) shows the x_2-r.m.s. of the differences in coefficients, gradients and heat flux difference at $t^* = 150$. Although the difference in coefficient value is high compared to that in the gradients, there is no correlation between the change in coefficient difference and the heat flux difference, whereas, the difference in gradients closely follows the heat flux. This indicates that the heat flux difference is proportional to the difference in gradients, and thereby governed by the gradients rather than the coefficients. Assuming that

$$\overline{C_A(\phi)\nabla A(\phi)} = \overline{C_A(\phi)}\ \overline{\nabla A(\phi)}, \tag{32}$$

then the heat flux difference, proportional to the difference in gradients, becomes

$$\overline{C_A}\ \overline{\nabla A} - C_A(\bar{\phi})\ \nabla A(\bar{\phi}) = \alpha(\overline{\nabla A} - \nabla A(\bar{\phi})). \tag{33}$$

This implies that

$$\overline{C_A} = C_A(\bar{\phi}) = \alpha \tag{34}$$

where α is a constant.

Although, having a constant coefficient value seems inconsistent with the afore-mentioned large difference in species mass coefficients (see fig. 4), this seemingly inconsistent result is understood if the coefficient value is examined. The difference in coefficients are only 2% of the coefficient values, hence they can be considered negligible. This finding highlights why the models proposed in the previous *a priori* study [18], focussing on the coefficient correction rather than the gradient terms, had limited success.

4.3 Modeling of the q-correction

As stated above, for the filtered energy equation, the filtered form of the heat flux term, i.e., for each component $\overline{\mathbf{q}_{IK}(\phi)} = \overline{C_A(\phi)\nabla A(\phi)}$, is needed. Since the unfiltered flow field is not known in LES, this term is calculated from the known filtered flow field instead, i.e., $\overline{\mathbf{q}_{IK}(\phi)} \approx \mathbf{q}_{IK}(\bar{\phi}) = C_A(\bar{\phi})\nabla A(\bar{\phi})$. The difference between the divergence of the filtered heat flux and the heat flux calculated from the filtered flow field is called heat flux (q) correction and is modeled in the present study. For this purpose, the unknown ϕ in the filtered heat flux formulation is approximated to $\phi^\star$, using the Approximate Deconvolution Method [20]. And the approximated ϕ, i.e., ϕ^*, is used for the calculation of the filtered heat flux.

Approximate Deconvolution Method

In the Approximate Deconvolution Method (ADM), the inverse of the filter operation is used to approximate to the unfiltered flow field. The inverse operator is constructed from an infinite series of filter operators. The reconstruction order, N, indicates the order of truncation [20]. The inverse operator is G^{-1},

$$G^{-1} \approx \sum_{\nu=0}^{N} (I - G)^N. \tag{35}$$

For example, if $N = 2$, the approximate value to the unfiltered flow field becomes:

$$\phi^\star \approx G^{-1} * \bar{\phi} = (I-G)^0 * \bar{\phi} + (I-G)^1 * \bar{\phi} + (I-G)^2 * \bar{\phi}, \tag{36}$$

$$\phi^\star = 3\bar{\phi} - 3\bar{\bar{\phi}} + \bar{\bar{\bar{\phi}}} + ... \tag{37}$$

Model Alternatives

The direct application of the ADM method would be to compute heat flux in $\overline{\mathbf{q}_{IK}(\phi)} = \overline{C_A(\phi)\nabla A(\phi)}$ using ϕ^* instead of ϕ, listed as M1 below. However, considering the possibility that this approach may not be applicable in the *a posteriori* studies, we investigate other model alternatives, listed as M2, M3, M4 and M6 below.

M 1

$$\overline{\mathbf{q}_{IK}(\phi)} = \overline{C_A(\phi^\star)\nabla A(\phi^\star)} \tag{38}$$

M 2

$$\overline{\mathbf{q}_{IK}(\phi)} = \overline{C_A(\phi^\star)}\ \ \overline{\nabla A(\phi^\star)} \tag{39}$$

M 3

$$\overline{\mathbf{q}_{IK}(\psi)} = \overline{C_A(\phi^\star)}\ \ \nabla A(\bar{\phi}) \tag{40}$$

M 4

$$\overline{\mathbf{q}_{IK}(\phi)} = C_A(\bar{\phi})\ \ \overline{\nabla A(\phi^\star)} \tag{41}$$

M 6

$$\overline{\mathbf{q}_{IK}(\psi)} = \overline{C_A(\bar{\phi})\nabla A(\bar{\phi})} \tag{42}$$

The domain r.m.s. activity study above is repeated for these model alternatives to measure their effectiveness. The results are tabulated in table 8 for $N = 2$. Note that the No Model case corresponds to the results of the previous section, and

that M6 is the same as the No Model except for the explicit filtering operation over the heat flux term. As clearly seen from table 8, the minimum difference, $\frac{\partial}{\partial x_j}\left(\overline{q_j(\phi)} - \overline{q_j(\phi^*)}\right)$, is obtained by using M1, followed by M2 and M4, as expected. These three models are approximately 30% better than the No Model case. The model M3 is the least satisfactory, yielding results no better than the No Model case. This again indicates the importance of the gradient reconstruction rather than that of the coefficients. The main deficiency of the No Model case is the calculation of the gradients from $\bar{\phi}$ as in M3. This can be partially avoided if the gradients are calculated from the approximated values instead, ϕ^*, as in M1, M2, M4.

The fact that models M2 and M4, which only differ in calculation of the coefficients, give similar results shows that different coefficient calculations have very little effect on the final solution, confirming the conclusions, as also confirmed by M3 and No Model solutions.

The evaluation of the models' performance is also conducted through an x_2-r.m.s. activity study for models M1 to M6 using a reconstruction order of $N = 5$. Figure 5 displays the difference between the filtered heat flux divergence and the heat flux divergence calculated from the filtered field at $t^* = 50,\ 150$. The results are consistent with the domain r.m.s. activity study; the best model is M1, followed by M2; M3 gave comparable results with the No Model case; M4 produces similar results with M2. Explicit filtering (M6) has a better performance than the No Model at $t^* = 50$, but not at $t^* = 150$.

Effect of model parameters

Order of reconstruction, N

It is reported in Stolz *et. al..* [21] that generally $N = 3$ gives acceptable approximations and $N > 5$ does not contribute much improvement. To investigate the effect of the N value for our case, the M1 approximation is obtained using various N values between 0 to 5. Note that $N = 0$ does not correspond to the No Model case, but to M6. The results are displayed in fig. 6. As expected, as N increases the discrepancy between the filtered and computed from the filtered solution heat flux term decreases. However, the improvement after $N = 3$ is minimal. Based on this analysis, we use $N = 3$ as the reconstruction order.

Reconstruction filter type

In Stolz *et. al..* [21], the approximate deconvolution is performed using a discrete Pade filter as opposed to the top hat filter used in our *a posteriori* studies. We inquire here how the approximation is affected by the chosen filter. We thus investigate the explicit filter of Stolz *et. al..* [21] along with three other filter formulations as follows

- **Filter A.** $G(\omega) = (1 + cos(\omega))/2$
- **Filter B.** $G(\omega) = (2 + cos(\omega))/3$
- **Filter C.** $G(\omega) = (10 + 8cos(\omega) - 2cos(2\omega))/16$
- **Filter D.** $G(\omega) = (16 - 2cos(3\omega) + 18cos(\omega))/32$,

and the transfer functions are shown in fig. 7.

Figure 8 displays the r.m.s. of the difference between the divergence of the filtered heat flux and that obtained from the model, i.e., $\nabla \cdot (\overline{q(\phi)} - \overline{q(\phi)}_{MODEL})$, where $q(\phi)$ is calculated on the coarse grid. For the No Model case $\overline{q(\phi)}_{MODEL} = q(\bar{\phi})$. The comparison is between the No Model data at time stations $t^* = 50,\ 150$ and the equivalent obtained from the model M1 using approximation order $N = 5$. In fig. 8(a), the largest and smallest deficits are obtained with Filters D and B, respectively. Considering that Filter B is not as dissipative as the others (see fig. 7), the smallest error with this filter is not surprising. When modeling is employed, more than half of the discrepancy in heat flux divergence is avoided for all filters. A similar trend is observed at $t^* = 150$, however, the need for q-correction is comparably low at this time step (see fig. 8(b)).

5 *A posteriori* analysis

The SGS-flux models used in the *a posteriori* study are the constant-coefficient Gradient (GRC), and the Scale Similarity (SSC) models, in addition to the dynamic Smagorinsky model in conjunction with the Yoshizawa model for the trace (SMD), and the mixed model using the dynamic Smagorinsky model in combination with the gradient model (MGRD). The GRC and SSC models are used with their calibrated coefficient values for $\bar{\Delta}/\Delta x_{DNS} = 8$ obtained from the corresponding DNS at $t^*_{tr} = 150$, as follows:

$$C_{GR} = 0.0910 \qquad \text{GRC}, \tag{43}$$

$$C_{SS} = 0.4009 \text{ for } \widehat{\bar{\Delta}} = 2\bar{\Delta} \qquad \text{SSC}. \tag{44}$$

Moreover, a coarse grid DNS is conducted (No Model) at the same resolution with that of the LES runs ($\Delta x_{LES} = 4\Delta x_{DNS}$). To investigate the effect of the q-correction, the same set of simulations are performed with the addition of the q-correction model M1 based on ADM [20] using reconstruction order $N = 3$ and Filter A. (ADM is not used as

an SGS-flux model but for modeling of the nonlinear heat flux term in the energy equation.) The results are compared both with the DNS and the filtered-and-coarsened (FC-DNS) data. The comparisons involve the x_2-r.m.s. activity of the divergence of the heat flux with and without q-correction, i.e., $\nabla \cdot \overline{q(\phi)}$ is compared with $\nabla \cdot q(\bar{\phi})$ and $\nabla \cdot \overline{q(\phi^*)}$. Moreover, the x_2-r.m.s. activity of the difference between the filtered heat flux divergence and the heat flux divergence calculated from the filtered field, i.e., $\nabla \cdot \overline{q(\phi)} - \nabla \cdot q(\bar{\phi})$ for the DNS flow field, and $\nabla \cdot \overline{q(\phi^*)} - \nabla \cdot q(\bar{\phi})$ for the approximated flow field, are examined; the former represents the q-correction required with each SGS-flux model since it compares data from simulations without q-correction, whereas, the latter shows the data obtained by implementing the q-correction model and indicates the amount of q-correction added.

Figure 9(a) shows the x_2-r.m.s. of the divergence of the heat flux calculated from the filtered DNS flow field (FCDNS, solid line), and that computed from the LES runs along with the filtered heat flux divergence obtained from the DNS data (filled square symbols). The results show that the target LES solution (FCDNS) overpredicts the filtered heat flux divergence, with a maximum of 20% at $x_2/\delta_{\omega,0} = 6$. In an actual LES run with the SGS-flux models employed in this study, the maximum overprediction in the layer becomes approximately 40% except for the SMD model for which it is 70% at $x_2/\delta_{\omega,0} = 2$. The heat flux divergence of the No Model solution is twice as large as the divergence of the filtered heat flux of the DNS, worse than any simulation with an SGS-flux model, indicating the significance of the SGS-flux modelling. The tails of the curves on the upper stream side are not well predicted with the similarity based models, sign of a close boundary location.

With the implementation of the heat flux model M1, it is possible to obtain better approximations for the filtered heat flux divergence of the DNS data, i.e, for the nonlinear term in the filtered energy equation. In fact, there is a clear improvement in the x_2-r.m.s. filtered heat flux divergence values for all simulations when M1 is employed (fig. 9(b)). Figures 9(a) and 9(b), where simulations with q-correction are abbreviated with HF, are plotted with the same scale to facilitate the comparison between models with and without q-correction. It must be noted that, M1 computes the divergence of the heat flux from the approximated flow field, ϕ^*, instead of the filtered flow field, $\bar{\phi}$. Thus, fig. 9(b) displays the heat flux divergence calculated from the approximated flow field, ϕ^*, for all simulations. Similarly, approximated flow field, ϕ^*, is obtained using the FCDNS data, $\bar{\phi}$, and the heat flux divergence is computed from this reconstructed flow field, abbreviated as RFCDNS in fig. 9(b). The addition of the heat flux model shifts the FCDNS curve down onto DNS, with less than 1% discrepancy. All simulations, including the No Model case, better predict the filtered DNS heat flux divergence after the addition of the heat flux model. The best prediction within the layer is obtained with the mixed model MGRD, and the maximum overprediction within the layer is with the SMD model. Close to the boundaries, errors are larger than inside the domain for all models but especially for the similarity based ones.

The x_2-r.m.s. difference of the filtered heat flux divergence and that calculated from the filtered flow field is shown in fig. 9(c). This quantity indicates the required q-correction with each SGS-flux model. The FCDNS data shows that even with an ideal LES, a q-correction equivalent to approximately 40% of the heat flux is needed, as also emphasized in the *a priori* tests. The SGS-flux model that least needs a q-correction is the GRC model, only slightly better than the other models. As expected, when no SGS-flux model is used (No Model simulation), the q-correction is needed more.

Fig. 9(d) displays the x_2-r.m.s. difference between the filtered heat flux divergence calculated from the approximated flow field and that calculated from the filtered flow field. This quantity represents the amount of q-correction actually added to the computations. Hence, the FCDNS curve is essentially that of fig. 9(c), consistent with the model performance observed for the FCDNS data. The q-correction added for all simulations is less than that is shown to be needed in fig. 9(c). The added correction for all the simulations except for the No Model compares with that added to FCDNS data. (Note that the r.m.s. of the difference (figs. 9(c), (d)) is larger than the difference of the r.m.s. shown in fig. 9(a) and (b)).

6 Conclusions

A Large Eddy Simulation (LES) study is conducted for a binary-species temporal mixing layer evolving at a free-stream pressure higher than the critical pressure of either fluid. Using an existing Direct Numerical Simulation (DNS) database, modeling needs for the small scale fluid behavior are identified and modeling strategies are determined. The proposed models are examined both in *a priori* and *a posteriori* tests.

The LES governing equations consist of the filtered DNS equations for conservation of mass, mo-

mentum, species and total energy coupled with a real-gas equation of state (EOS). The transport properties are functions of the thermodynamic variables. To close the filtered equations, SGS-flux models are employed. The models used for the typical SGS-flux terms encompasses the constant coefficient Gradient (GRC) and Scale Similarity (SSC) models, the dynamic Smagorinsky model (SMD), and the mixed model where the dynamic Smagorinsky is combined with the Gradient model (MGRD). In addition to the typical SGS-flux closures, a heat flux (q) correction model is developed following the findings of an earlier *a priori* investigation[18]. The heat flux model is different than that proposed by Selle *et. al.*.[18], and based on Approximate Deconvolution Method of Stolz *et. al.*[20].

The newly proposed q-correction model is assessed both in the *a priori* and *a posteriori* tests by comparing results with the filtered-and-coarsened DNS (FC-DNS). In the revisited *a priori* analysis, it is found that the q-correction is larger in the earlier stages of the layer development. To understand the aport of each contribution to the heat flux that is in the form of a coefficient multiplied by a gradient, the difference in the divergence of the filtered heat flux and that calculated from the filtered flow field is examined for each contribution. It is observed that the main cause of the difference is due to the concentration gradients (Dufour component). In addition, it is concluded that the q-correction model must improve the gradient representations on the coarse grid rather than the corresponding coefficient values. Analyses for the selection of the reconstruction filter type and reconstruction order are conducted, different variations of the main heat flux model are tested and their results are examined *a priori*. The final q-correction model chosen for the *a posteriori* tests improved the heat flux representation $\approx 60\%$, and $\approx 20\%$ at $t^* = 50, 150$, respectively, in the *a priori* analysis. The *a posteriori* tests also showed an improvement, albeit lower than that of *a priori* tests.

Acknowledgments

This study was conducted at the Jet Propulsion Laboratory (JPL) of the California Institute of Technology (Caltech) under the sponsorship of the U.S. Air Force Office of Scientific Research (AFOSR) with Dr. Julian Tishkoff serving as technical director, under an agreement with the National Aeronautics and Space Administration, and of an AFOSR Grant to Caltech under the technical direction of Drs. Mitat Birkan, Doug Talley (of Edwards Air Force Research Laboratories (AFRL)), Tim Edwards and Cam Carter (both of Wright Patterson AFRL). Dr. Nora Okong'o is thanked for very helpful discussions on numerical techniques. The computational resources were provided by the JPL Supercomputing Center.

References

[1] Bardina, J., Ferziger, J. and Reynolds, W. AIAA 80-1357, 1980.

[2] Clark, R., Ferziger, J., and Reynolds, W. *J. Fluid Mech.*91(1):1–16, 1979.

[3] Germano, M., Piomelli, U., Moin, P. & Cabot, W. *Phys. Fluids A*3 (7):1760–1765, 1991.

[4] Hannoun, I. A., Fernando, H. J. S. and List, E. J. *J. Fluid Mech.* 189:189-209, 1988.

[5] Harstad, K., Miller, R. S. and Bellan, J. *A.I.Ch.E. J.*, 43(6):1605-1610, 1997.

[6] Harstad, K. and Bellan, J. *Int. J. Heat Mass Transfer*41:3537–3550, 1998.

[7] Harstad, K. and Bellan, J. *Int. J. Multiphase Flow* 26(10):1675–1706, 2000.

[8] Keizer, J.*Statistical Thermodynamics of Nonequilibrium Processes*Springler-Verlag, New York, 1987.

[9] Lilly, D.*Physics of Fluids A*4 (3):633–635, 1992.

[10] Liu, S., Meneveau, C. and Katz, J. *J. Fluid Mech.*275:83–119, 1994.

[11] Miller, R., Harstad, K. and Bellan, J. *J. Fluid Mech.* 436:1–39, 2001.

[12] Okong'o, N. and Bellan, J. *J. Fluid Mech.* 464:1–34, 2002.

[13] Okong'o, N. and Bellan, J. *J. Fluid Mech.* 499:1–47, 2004.

[14] Okong'o, N., Harstad, K. and Bellan, J. *AIAA J.* 40(5):914–926, 2002.

[15] Oschwald, M. and Schik, A. *Exp. Fluids* 27:497–506, 1999.

[16] Prausnitz, J., Lichtenthaler, R. and de Azevedo, E. *Molecular Thermodynamics for Fluid-Phase Equilibrium* Prentice-Hall, 1986.

[17] Pruett, C., Sochacki, J. and Adams, N. *Phys. Fluids* 13(9):2578–2589, 2001.

[18] Selle, L. C., Okong'o, N. A., Bellan, J. and Harstad, K. G. *J. Fluid Mech.* 593:57-91, 2007.

[19] Smagorinksy, J. *Large Eddy Simulation of Complex Engineering and Geophysical Flows*, edited by B. Galperin and S. Orszag, chap. 1, Cambridge University Press, 3–36, 1993.

[20] Stolz, S., Adams, N. A. *Phys. Fluids* 11(7):1699–1701, 1999.

[21] Stolz, S., Adams, N. A., and Keiser, L. *Phys. Fluids* 13(4):997–1015, 2001.

[22] Vreman, B., Geurts, B. and Kuerten, H. *J. Fluid Mech.* 339:357-390, 1997.

[23] Yoshizawa, A. *Phys. Fluids* 29(7):2152–2164, 1986.

Species	m (g/mol)	T_c (K)	p_c(MPa)
H_2	2.016	33.0	1.284
O_2	31.999	154.6	5.043

Table 1. Pure species properties.

Transport property	Model
$\mu = \mu_R \left(T/T_R\right)^n$	$n = 0.75$
$Sc \equiv \mu/\left(\rho \alpha_D D\right)$	$\left[\begin{array}{c}\left(1.334 - 0.668Y_2 - 0.186Y_2^2 - 0.268Y_2^6\right) \\ \times \left[1 + \left(88.6/T\right)^{1.5}\right]\end{array}\right]$
$\Pr \equiv \mu C_p/\left(m\lambda\right)$	$1.335/T^{0.1}$
α_{IK} or α_{BK}	$\alpha_{BK} = 0.2$
T Range	200K–800K
p Range	∼100atm

Table 2. Transport properties for O_2/H_2 binary mixture. $T_R = (T_1 + T_2)/2$, T in Kelvin. α_{IK} from Harstad & Bellan (2000), and α_{BK} from Harstad & Bellan (1998) and Harstad & Bellan (2001).

Run	OH750	OH550	OH500
Species 2	O_2	O_2	O_2
Species 1	H_2	H_2	H_2
$T_2; T_1$ (K)	400;600	400;600	235;287
ρ_2/ρ_1	24.40	24.40	24.51
p_0 (atm)	100	100	100
Re_0	750	550	500
$\lambda_1/\delta_{\omega,0}$	7.29	10.35	10.61
L_1 (m)	0.200	0.284	0.284
L_2 (m)	0.200	0.284	0.284
L_3 (m)	0.120	0.170	0.170
Δx (10^{-4}m)	5.77	8.19	8.39
$F_{2D}; F_{3D}$	0.1;0.05	0.1;0.025	0.1;0.025
t^*_{tr}	150	270	290
$\mathrm{Re}_{m,tr}$	1507	1907	1772

Table 3. Simulation parameters for supercritical temporal mixing layer O_2H_2 database. λ_1 is the streamwise perturbation wavelength and F_{2D} and F_{3D} are the streamwise and spanwise perturbation amplitudes. All simulations have $M_{c.0} = 0.4$, $L_1 = 4\lambda_1$ and $L_3 = 0.6L_1$. $\Delta x = \max(\Delta x_1, \Delta x_2, \Delta x_3)$.

	x_1 Momentum	$t^* = 25$	$t^* = 50$	$t^* = 100$	$t^* = 150$
	$\frac{\partial}{\partial x_j}\left(\bar{\rho}\tilde{u}_1\tilde{u}_j\right)$	13.69	16.97	18.02	16.30
	$\frac{\partial}{\partial x_1}\left[p\left(\bar{\phi}\right)\right]$	9.61	12.24	10.47	9.32
	$\frac{\partial}{\partial x_j}\left[\sigma_{1j}\left(\bar{\phi}\right)\right]$	2.76	3.11	2.98	2.19
	$\frac{\partial}{\partial x_j}\left(\bar{\rho}\tau_{1j}\right)$	1.48	2.39	2.06	1.60
	$\frac{\partial}{\partial x_j}\left[\Delta\left(\bar{\sigma}_{1j}\right)\right]$	1.06	1.44	1.08	0.69
*	$\frac{\partial}{\partial x_1}\left[\Delta\left(\bar{p}\right)\right]$	0.42	0.73	0.57	0.44

$$\Delta\left(\bar{f}\right) \equiv \overline{f\left(\phi\right)} - f\left(\bar{\phi}\right)$$

Table 4. Magnitude (r.m.s.) of terms in LES equations at various time steps for O_2H_2 with $Re = 750$ for $\bar{\Delta} = 8\Delta x$. Units are $10^6\mathrm{Nm}^{-3}$.

	x_2 Momentum	$t^* = 25$	$t^* = 50$	$t^* = 100$	$t^* = 150$
	$\frac{\partial}{\partial x_j}\left(\bar{\rho}\tilde{u}_1\tilde{u}_j\right)$	6.21	10.33	12.37	12.23
	$\frac{\partial}{\partial x_1}\left[p\left(\bar{\phi}\right)\right]$	6.90	9.75	11.14	10.33
	$\frac{\partial}{\partial x_j}\left(\bar{\rho}\tau_{1j}\right)$	0.63	1.82	1.70	1.30
	$\frac{\partial}{\partial x_j}\left[\sigma_{1j}\left(\bar{\phi}\right)\right]$	0.42	1.25	1.49	1.17
*	$\frac{\partial}{\partial x_1}\left[\Delta\left(\bar{p}\right)\right]$	2.12	2.07	1.61	1.02
	$\frac{\partial}{\partial x_j}\left[\Delta\left(\bar{\sigma}_{1j}\right)\right]$	0.19	0.54	0.50	0.25

$$\Delta\left(\bar{f}\right) \equiv \overline{f\left(\phi\right)} - f\left(\bar{\phi}\right)$$

Table 5. Magnitude (r.m.s.) of terms in LES equations at various time steps for O_2H_2 with $Re = 750$ for $\bar{\Delta} = 8\Delta x$. Units are $10^6\mathrm{Nm}^{-3}$.

	x_3 Momentum	$t^* = 25$	$t^* = 50$	$t^* = 100$	$t^* = 150$
	$\frac{\partial}{\partial x_j}\left(\bar{\rho}\tilde{u}_1\tilde{u}_j\right)$	2.07	5.38	9.05	9.01
	$\frac{\partial}{\partial x_1}\left[p\left(\bar{\phi}\right)\right]$	2.81	5.75	7.19	6.82
*	$\frac{\partial}{\partial x_1}\left[\Delta\left(\bar{p}\right)\right]$	2.13	2.00	1.61	1.08
	$\frac{\partial}{\partial x_j}\left(\bar{\rho}\tau_{1j}\right)$	0.22	1.08	1.23	0.98
	$\frac{\partial}{\partial x_j}\left[\sigma_{1j}\left(\bar{\phi}\right)\right]$	0.15	0.52	0.87	0.94
	$\frac{\partial}{\partial x_j}\left[\Delta\left(\bar{\sigma}_{1j}\right)\right]$	0.06	0.18	0.23	0.18

$$\Delta\left(\bar{f}\right) \equiv \overline{f\left(\phi\right)} - f\left(\bar{\phi}\right)$$

Table 6. Magnitude (r.m.s.) of terms in LES equations at various time steps for O_2H_2 with $Re = 750$ for $\bar{\Delta} = 8\Delta x$. Units are $10^6\mathrm{Nm}^{-3}$.

Energy	$t^* = 25$	$t^* = 50$	$t^* = 100$	$t^* = 150$
$\frac{\partial}{\partial x_j}\left[q_{IKj}\left(\bar{\phi}\right)\right]$	30.34	43.88	43.14	33.64
$\frac{\partial}{\partial x_j}\left(\bar{\rho}\tilde{e}_t\tilde{u}_j\right)$	27.07	44.33	42.64	33.44
$\frac{\partial}{\partial x_j}\left(\bar{\rho}\zeta_j\right)$	16.71	30.20	26.51	18.97
$\frac{\partial}{\partial x_j}\left[p\left(\bar{\phi}\right)\tilde{u}_j\right]$	11.24	18.31	17.61	13.80
$\frac{\partial}{\partial x_j}\left[\Delta\left(\bar{q}_{IKj}\right)\right]$	12.25	21.46	16.75	10.15
$\frac{\partial}{\partial x_j}\left[\sigma_{ij}\left(\bar{\phi}\right)\tilde{u}_i\right]$	1.19	1.31	1.29	0.78
$\frac{\partial}{\partial x_j}\left(\overline{\rho}\tau_{ij}\widetilde{u}_i\right)$	0.33	0.61	0.53	0.38
$\frac{\partial}{\partial x_j}\left[\Delta\left(\overline{\sigma_{ij}u_i}\right)\right]$	0.45	0.66	0.54	0.28
$\frac{\partial}{\partial x_j}\left(\overline{\rho}\kappa_j - \overline{\rho}\tau_{ij}\widetilde{u}_i\right)$	0.13	0.22	0.11	0.07
$\frac{\partial}{\partial x_j}\left\{\Delta\left(\bar{p}\right)\tilde{u}_j\right\}$	0.11	0.16	0.11	0.07

$$\Delta\left(\bar{f}\right) \equiv \overline{f\left(\phi\right)} - f\left(\bar{\phi}\right)$$

Table 7. Magnitude (r.m.s.) of terms in LES equations at t^*_{tr}. Units are $10^9\mathrm{Jm}^{-3}\mathrm{s}^{-1}$.

		$t^* = 25$	$t^* = 50$	$t^* = 100$	$t^* = 150$
No Model	$\frac{\partial}{\partial x_j}\left(\overline{q_j\left(\phi\right)} - q_j\left(\bar{\phi}\right)\right)$	12.25	21.46	16.75	10.15
M 1	$\frac{\partial}{\partial x_j}\left(\overline{q_j\left(\phi\right)} - \overline{q_j\left(\phi^*\right)}\right)$	4.05	7.44	5.46	3.13
M 2	$\frac{\partial}{\partial x_j}\left(\overline{q_j\left(\phi\right)} - \overline{q_j\left(\phi^*\right)}\right)$	6.66	10.80	7.16	3.25
M 3	$\frac{\partial}{\partial x_j}\left(\overline{q_j\left(\phi\right)} - \overline{q_j\left(\phi^*\right)}\right)$	11.64	20.52	16.18	9.94
M 4	$\frac{\partial}{\partial x_j}\left(\overline{q_j\left(\phi\right)} - \overline{q_j\left(\phi^*\right)}\right)$	7.74	12.25	8.10	3.47

Table 8. Comparison of the modeled filtered heat flux term obtained with the model approximations in eqns 38- 42 at various time steps using eqn 37 for O_2H_2 with $Re = 750$ for $\bar{\Delta} = 8\Delta x$. Units are $10^9\mathrm{Jm}^{-3}\mathrm{s}^{-1}$.

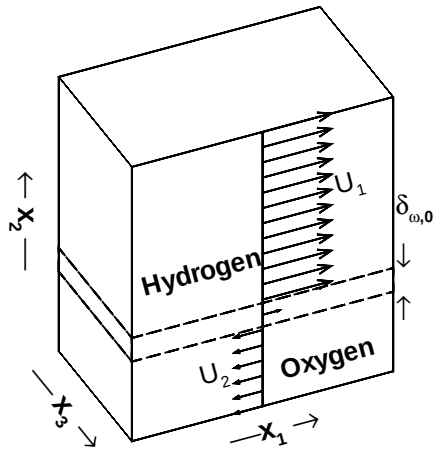

Figure 1. O_2/H_2 mixing layer configuration.

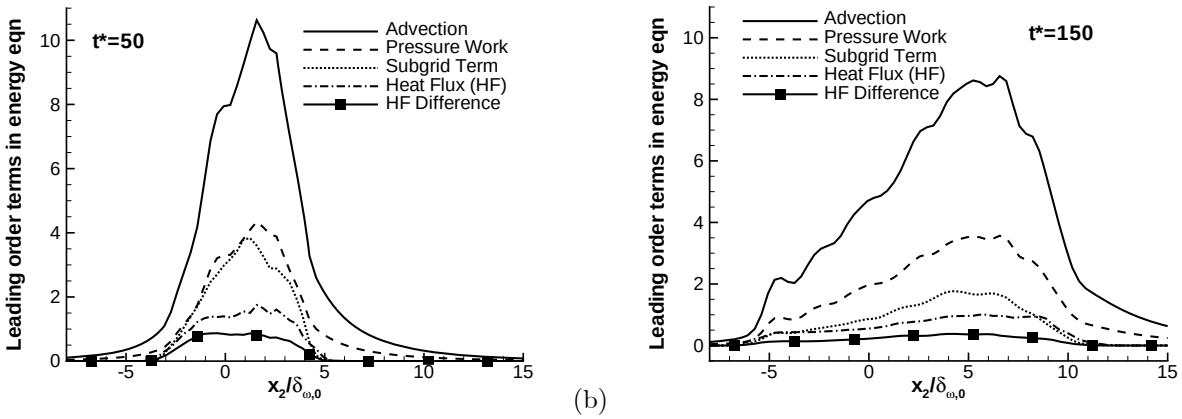

Figure 2. The x_2 r.m.s. of the leading order terms in the energy equation at $t^* = 50,\ 150$.

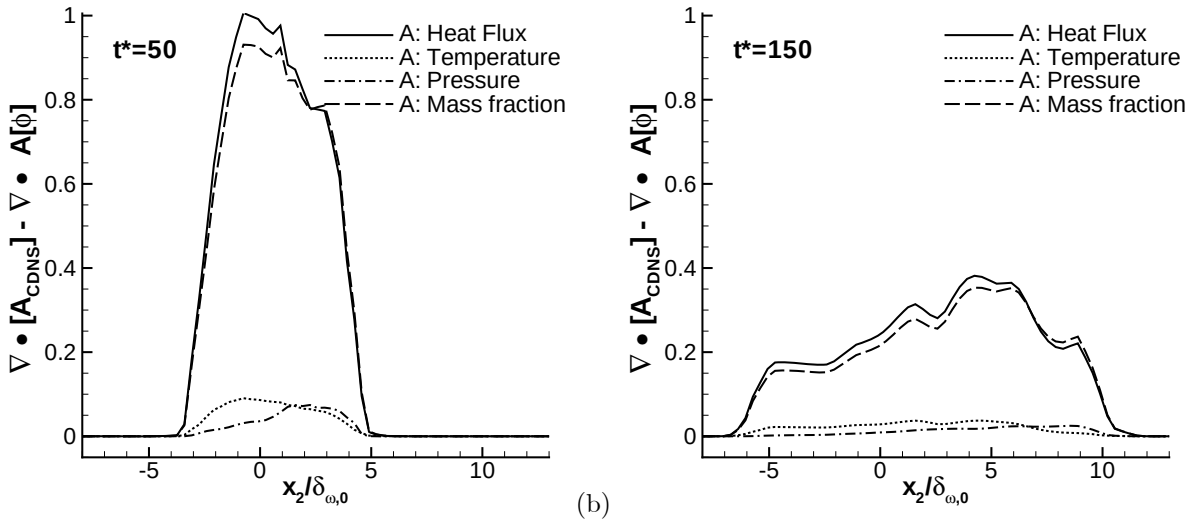

Figure 3. The x_2 r.m.s. of the difference of the heat flux and its each component at $t^* = 50, 150$. For filtering operation square brackets are used.

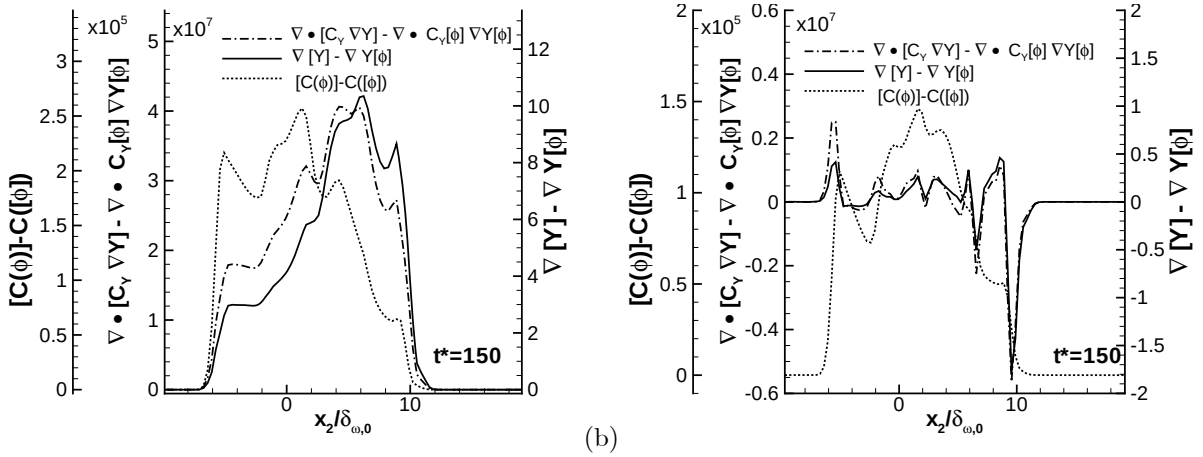

Figure 4. Comparison of the difference in coefficients, gradients, and the heat fluxes, (a) r.m.s, (b) mean at $t^* = 150$. For filtering operation square brackets are used.

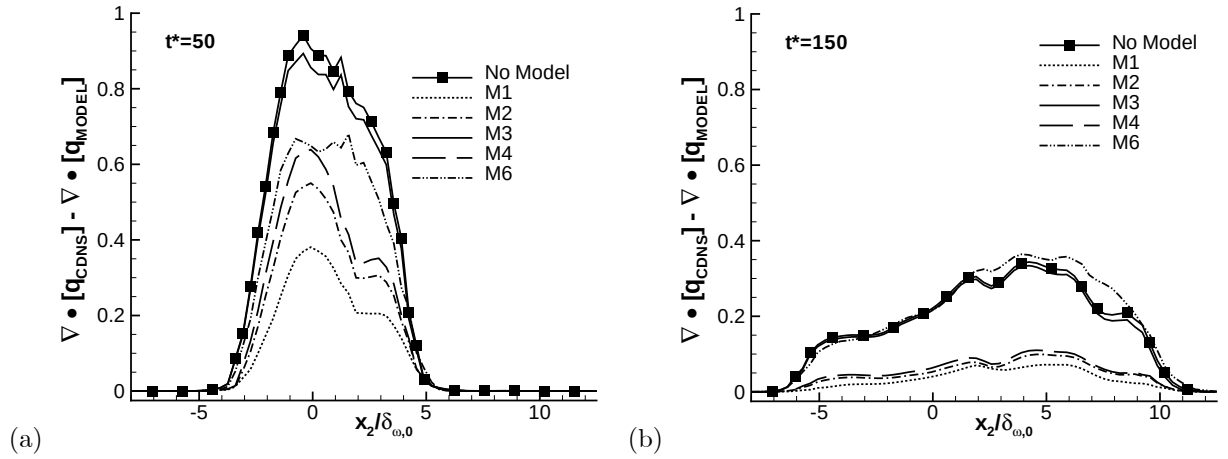

Figure 5. The x_2 r.m.s. of the difference of heat flux divergence obtained with various model formulations at $t^* = 50,\ 150$. The data shown is normalized with 6.5×10^{10}. For filtering operation square brackets are used.

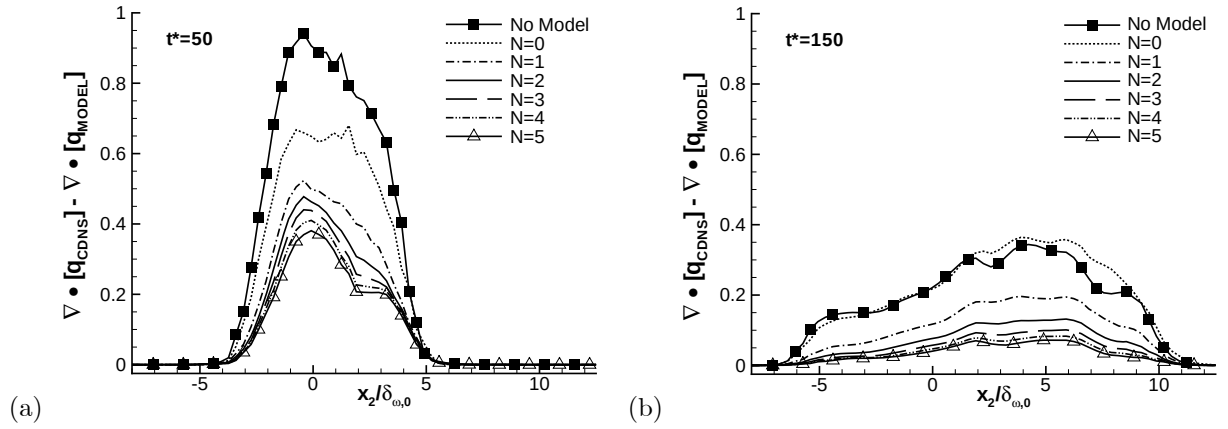

Figure 6. Effect of order of reconstruction on heat flux correction term. The data shown is normalized with 6.5×10^{10}. For filtering operation square brackets are used.

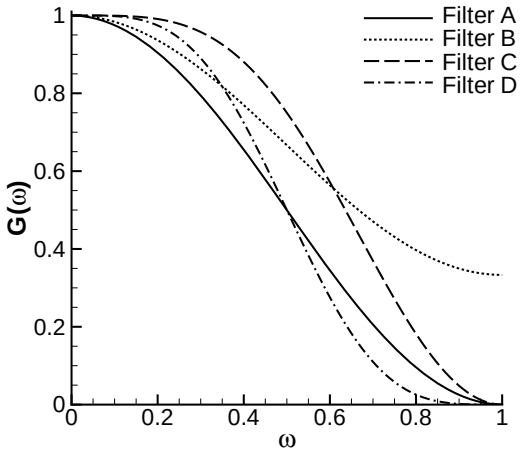

Figure 7. Transfer functions of the filters tested.

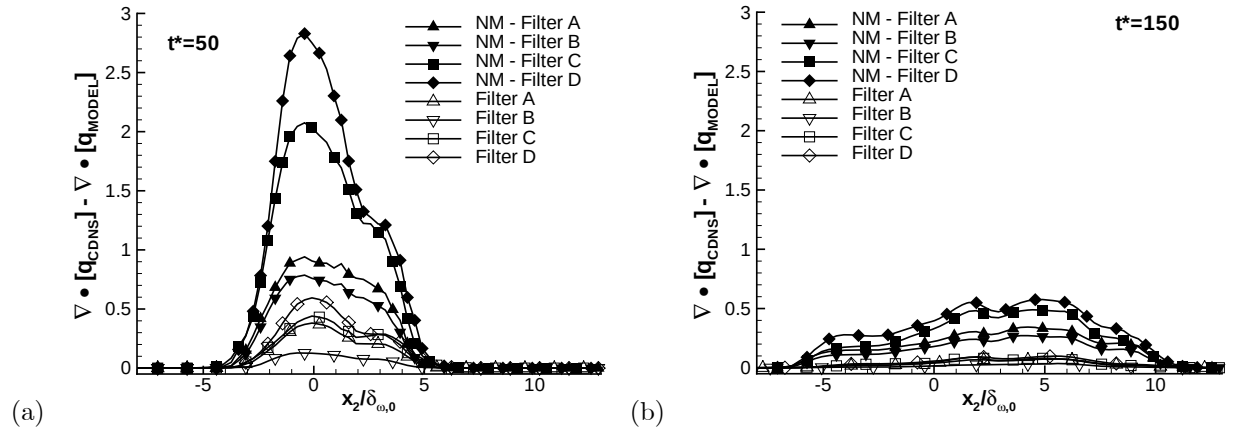

Figure 8. The x_2 r.m.s. of the difference of heat flux divergence at $t^* = 50,\ 150$. The data shown is normalized with 6.5×10^{10}. For filtering operation square brackets are used.

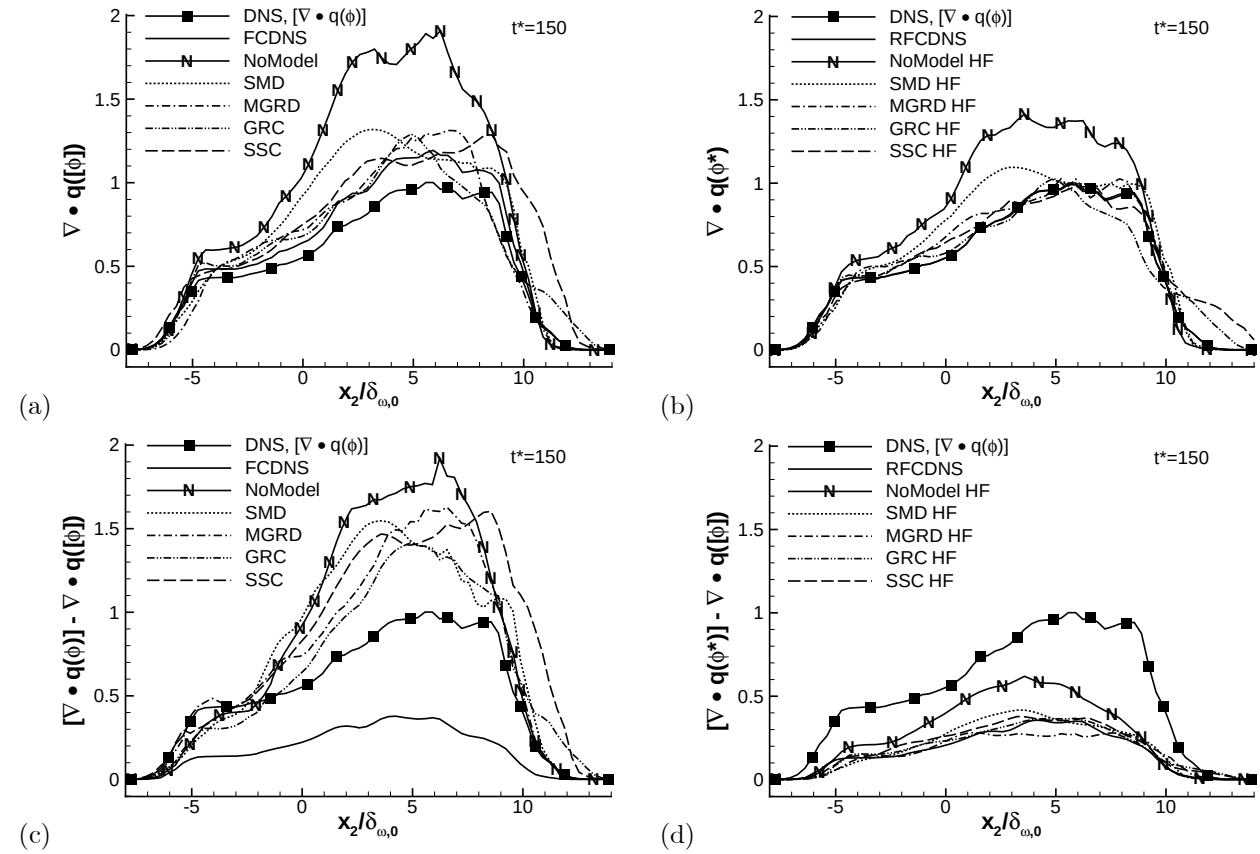

Figure 9. (a), (b); The x_2 r.m.s. of the divergence of the heat flux calculated from the filtered flow field (a), calculated from the approximated flow field (b). (c), (d); The x_2 r.m.s. of the difference of the filtered heat flux divergence and that calculated from the filtered flow field (c), The x_2 r.m.s. of the difference of the filtered heat flux divergence calculated from the approximate flow field and that calculated from the filtered flow field (d). (a), (c) without q-correction, (b), (d) with q-correction model M1, using various SGS-flux models at $t^* = 150$. The data shown is normalized with 6.5×10^{10}. For filtering operation square brackets are used.